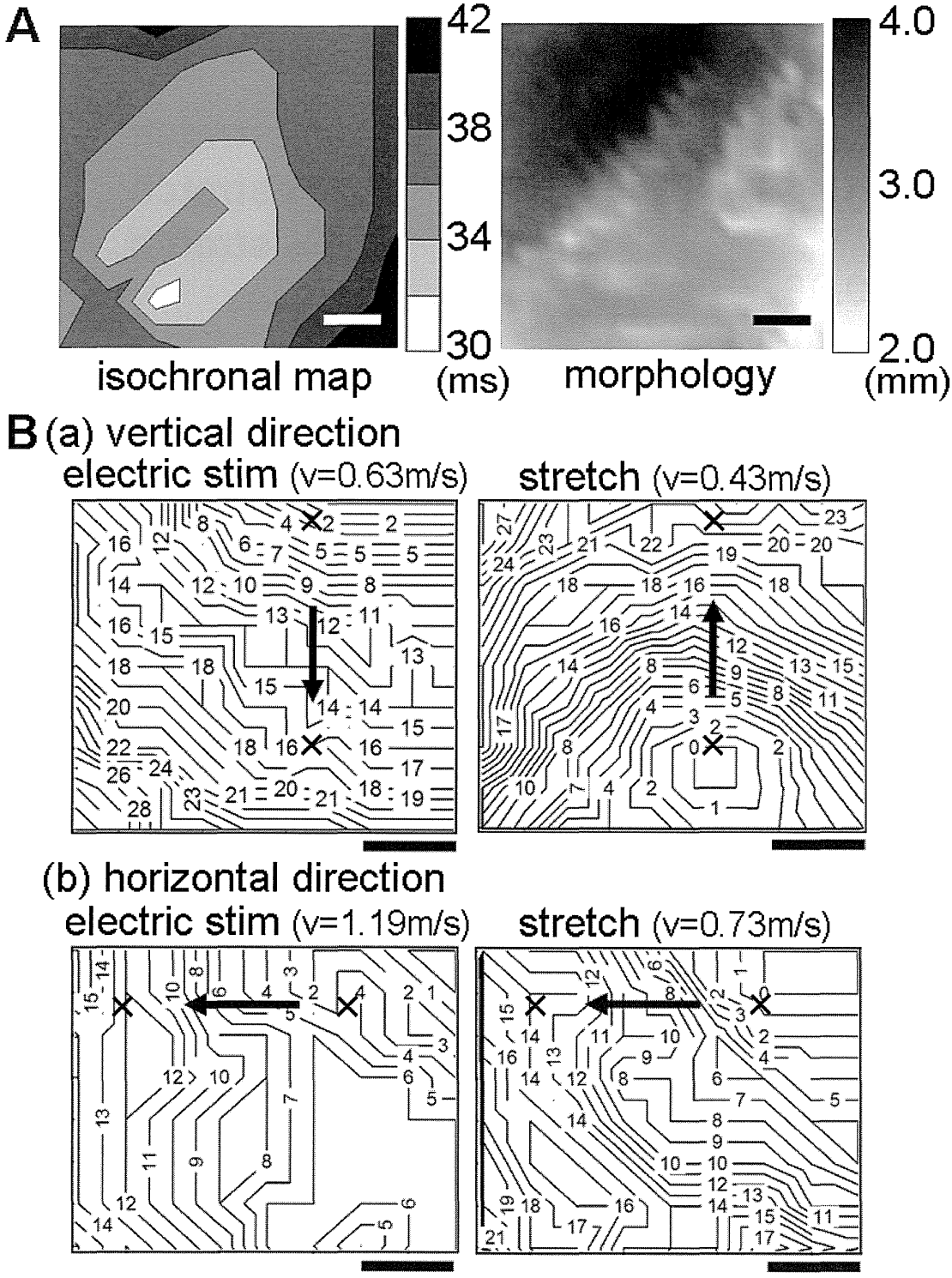


**Online Figure VI**

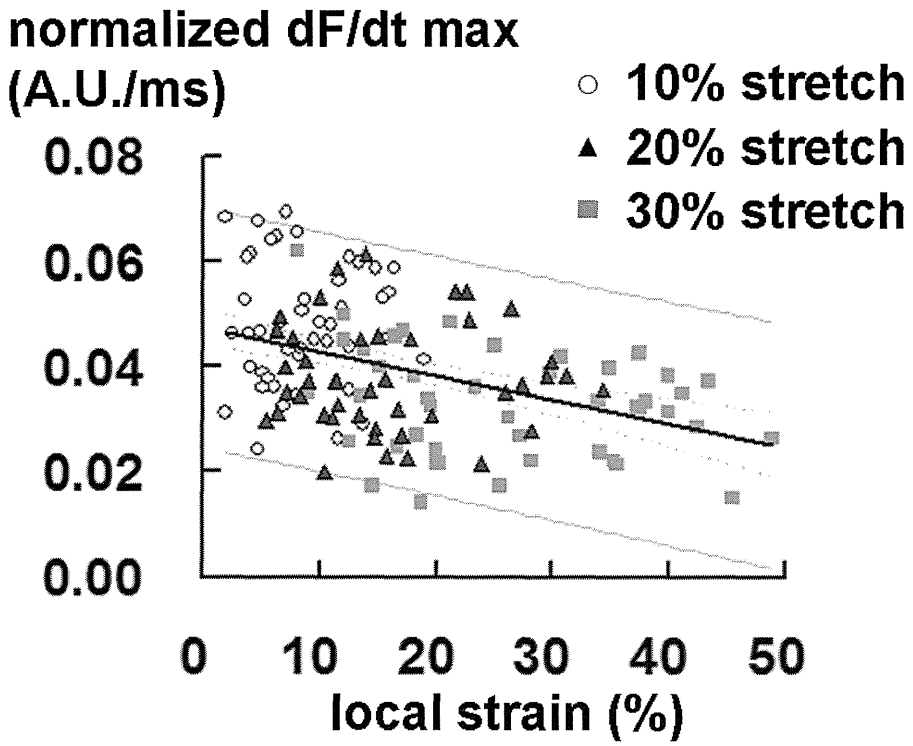


**Online Figure VII**

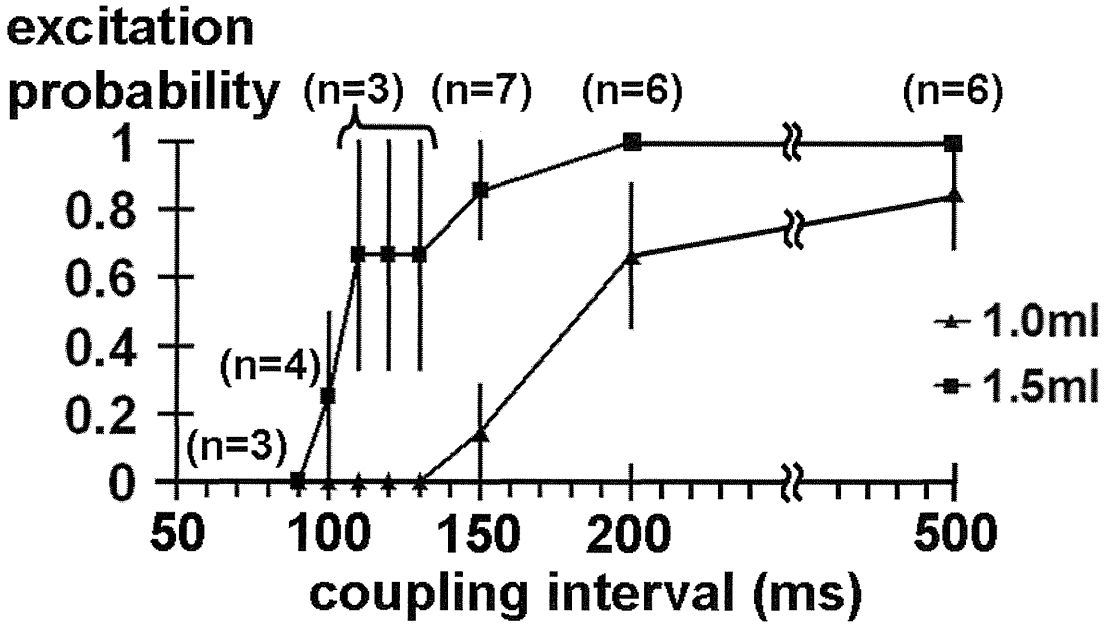


**Online Figure VIII**

Comput Mech (2010) 46:247–258
DOI 10.1007/s00466-009-0432-1

ORIGINAL PAPER

# Study of efficient homogenization algorithms for nonlinear problems

## Approximation of a homogenized tangent stiffness to reduce computational cost

**Jun-ichi Okada · Takumi Washio · Toshiaki Hisada**

Received: 30 January 2009 / Accepted: 10 October 2009 / Published online: 31 October 2009


**Abstract** A framework for the homogenization of nonlinear problems is discussed with respect to block LU factorization of the micro–macro coupled equation, and based on the relation between the characteristic deformation and the Schur-Complement as the homogenized tangent stiffness. In addition, a couple of approximation methods are introduced to reduce the computational cost, i.e., a simple scheme to reuse the old characteristic deformation and a sophisticated method based on the mode-superposition method developed by our group. Note that these approximation methods satisfy the equilibrium conditions in both scales. Then, using a simplified FE model, the conventional algorithm, a relative algorithm originating from the block LU factorization, and the above-mentioned algorithms with the approximated Schur-Complement are compared and discussed. Finally, a large-scale heart simulation using parallel computation is presented, based on the proposed method.

**Keywords** Homogenization method · Nonlinear finite element analysis · Schur-Complement · Mode superposition · Parallel computation · Block LU factorization · Heart

### List of symbols

| | |
|---|---|
| $\mathbf{Y}, \mathbf{y}$ | Position vector around the deformation in the microstructure |
| $\mathbf{X}, \mathbf{x}$ | Position vector around the deformation in the macrostructure |
| $\mathbf{u}$ | Macroscopic displacement vector |
| $\{\mathbf{u}\}$ | Macroscopic structure nodal displacement vector |
| $\{\mathbf{u}^e\}$ | Macroscopic structure nodal displacement vector per element |
| $\mathbf{w}$ | Periodic component of the microscopic displacement vector |
| $\{\mathbf{w}\}$ | Periodic component of the nodal displacement vectors of all microstructures |
| $\{\mathbf{w}^Q\}$ | Periodic component of the nodal displacement vector of a single microstructure |
| $\{\mathbf{w}^e\}$ | Periodic component of the nodal displacement vector per element |
| $\mathbf{F}$ | The deformation gradient tensor |
| $\mathbf{Z}$ | The displacement gradient tensor |
| $\mathbf{C}$ | The right Cauchy–Green tensor |
| $\mathbf{E}$ | The Green–Lagrange strain tensor |
| $\Pi$ | The first Piola–Kirchhoff stress tensor |
| $\mathbf{I}$ | The identity tensor |
| $I_c, II_c, III_c$ | Principal invariants |
| $J$ | Determinant $\mathbf{F}$ |

## 1 Introduction

The door to petaflop computing has recently opened and meaningful applications for massively parallel computers are being sought. A multi-scale approach to biomechanical problems is consequential in the post-genome era and the homogenization method is going to play a more important role than ever before. The homogenization method is a mathematical modeling technique for efficiently analyzing inhomogeneous material with a periodic microstructure. In

J. Okada (✉) · T. Washio · T. Hisada
Graduate School of Frontier Sciences, University of Tokyo,
5-1-5 Kashiwanoha, Kashiwa, Chiba 277-8563, Japan
e-mail: okada@sml.k.u-tokyo.ac.jp

biomaterial, the periodicity hypothesized in the homogenization method is not strictly established. However, Terada et al. [1] have shown that an appropriate equivalent characteristic is obtained in material with an irregular microstructure by assuming a periodic boundary condition. Thus, it is possible to evaluate the effect of each component in the microstructure on the macroscopic behavior, if microstructure modeling is appropriate. The homogenization method for biomaterial was applied to bone by Hollister and Kikuchi [2], while a two-dimensional analysis of engineered tissue cells was conducted by Breuls et al. [3]. In an example using the heart, Krassowska et al. [4] applied the method to an excitation propagation phenomena. To investigate the effect of intracellular structure on heartbeat, the authors have developed the necessary finite element homogenization method, where the heart is the macrostructure and the cardiomyocyte the microstructure. Thus the problem inevitably becomes a large-scale one.

In the homogenization method two scales are introduced, namely, a scale for the unit period, and a scale for the whole material. By solving the governing equations for both scales with coupling, we can obtain the macroscopic characteristic as an equivalent homogeneous body and variable distribution from the microstructure. In the conventional nonlinear homogenization method [5,6], it is first necessary to calculate microscopic equilibrium and then the macroscopic tangential homogenization updates all quadrature points at every Newton–Raphson iteration, resulting in huge computational cost. Even with a high performance computer, the cost is prohibitive for practical large-scale problems. To reduce this computational cost, various techniques have been devised. These include, for example, the construction of a database with the homogenized properties [7], sensitivity analysis [8], Fast Fourier Transforms [9], and so on. In a previous work, we proposed a homogenization method using characteristic deformation mode superposition [10,11]. This is, however, an approximation method and the accuracy depends on the problem. We subsequently proposed a new algorithm that solves the microscopic equilibrium equation alternately with the solution of the mode superposition-based micro–macro coupled equation. In this algorithm, the equilibrium conditions for both the micro and macro structures are satisfied with far less computational cost. This method is applicable to microstructures composed of slightly incompressible and viscoelastic materials [12–15].

Looking at this method from the block LU factorization of the micro–macro coupled equation, we recognize that the Schur-Complement as the homogenized tangent stiffness, is ingeniously approximated with the aid of mode superposition. It is further beneficial to generalize this view, that is, to interpret the framework of the homogenization method with regard to the block LU factorization and investigate how the Schur-Complement can be approximated to reduce the computational cost whilst preserving the accuracy. Accordingly, a couple of approximation methods, i.e., a simple scheme to reuse the old characteristic deformation and the above-mentioned mode-superposition based method, are introduced in this paper. Then a simplified numerical example is solved using both the conventional homogenization algorithm and the algorithm originating from the block LU factorization, and the performance of each is discussed. Finally, a large-scale heart simulation using parallel computation is presented based on the proposed method.

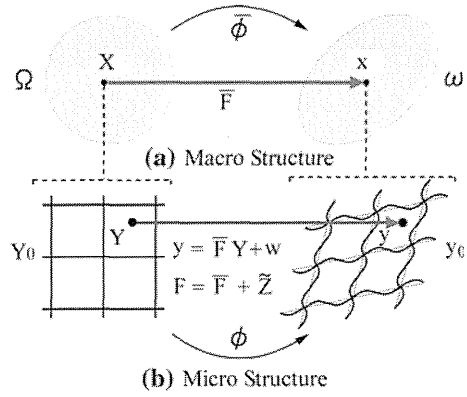


**Fig. 1** Homogenization method for large deformation problems. **a** Macro structure. **b** Micro structure

## 2 Homogenization method for finite deformation problem

### 2.1 Problem statement and geometric prospect

We assume that the material in the body ($\Omega$) reveals heterogeneity on a very fine scale and is characterized by the periodic distribution of a basic structural element ($Y_0$) as shown in Fig. 1. To measure the changes in the spatial domains, we introduce two scales: a macro-scale $X \in \Omega$ and a micro-scale $Y \in Y_0$. Thus the actual domain can be regarded as the product space ($\Omega \times Y_0$). In the subsequent development, the macroscopic quantity corresponding to the microscopic one is expressed with a bar symbol over the microscopic symbol. The following assumptions of homogenization are applied in the formulation of the homogenization method.

- A macrostructure that consists of a periodic microstructure can be considered to be an approximately equivalent homogeneous substance.
- A microstructure is infinitely fine compared with a macrostructure; the variable defined at each point of the macrostructure corresponds to the volume average of the variables in the microstructure.

It is assumed that the deformation of the microstructure is linked to the local values of the macro continuum via

$$\mathbf{y} = \overline{\mathbf{F}}\mathbf{Y} + \mathbf{w}, \tag{1}$$

where $\mathbf{y}$ and $\mathbf{Y}$ are position vectors defined on the microstructure [16].

The deformation consists of a homogeneous part $\overline{\mathbf{F}}\mathbf{Y}$ and a non-homogeneous superposed field $\mathbf{w}$. Consequently, the following relationships exist between the microscopic and macroscopic deformation gradients.

$$\mathbf{F} = \nabla_Y \mathbf{y} = \frac{\partial \mathbf{y}}{\partial \mathbf{Y}} = \overline{\mathbf{F}} + \tilde{\mathbf{Z}}, \tag{2}$$

$$\overline{\mathbf{F}} = \nabla_X \mathbf{x} = \frac{\partial \mathbf{x}}{\partial \mathbf{X}}, \tag{3}$$

$$\tilde{\mathbf{Z}} = \nabla_Y \mathbf{w} = \frac{\partial \mathbf{w}}{\partial \mathbf{Y}}. \tag{4}$$

Thus increment and variation of the deformation gradients are represented, respectively, as

$$\Delta\mathbf{F} = \Delta\overline{\mathbf{F}} + \Delta\tilde{\mathbf{Z}} = \Delta\overline{\mathbf{F}} + \nabla_Y \Delta\mathbf{w}, \tag{5}$$

$$\delta\mathbf{F} = \delta\overline{\mathbf{F}} + \delta\tilde{\mathbf{Z}} = \delta\overline{\mathbf{F}} + \nabla_Y \delta\mathbf{w}. \tag{6}$$

For the assumptions mentioned above, the macroscopic gradients are related via the volume averages

$$\overline{\mathbf{F}} = \frac{1}{|V|}\int_{Y_0} \mathbf{F} dY = \frac{1}{|V|}\int_{Y_0} (\overline{\mathbf{F}} + \tilde{\mathbf{Z}}) dY = \overline{\mathbf{F}} + \frac{1}{|V|}\int_{Y_0} \tilde{\mathbf{Z}} dY, \tag{7}$$

where $V$ is the volume of the microstructure $Y_0$. Then, the fluctuation field $\mathbf{w}$ must satisfy the constraint

$$\int_{Y_0} \tilde{\mathbf{Z}} dY = \int_{Y_0} \frac{\partial \mathbf{w}}{\partial \mathbf{Y}} dY = \int_{\partial Y_0} \mathbf{N} \otimes \mathbf{w} dS = \mathbf{0}, \tag{8}$$

where $\mathbf{N}$ is an outward normal vector on the boundary $\partial Y_0$. This constraint is satisfied when $\mathbf{w}$ is periodic.

### 2.2 Formulation of homogenization method and finite element discretization

We now consider the equilibrium of material with a periodic microstructure, modeled by hyperelastic material. Using the principle of stationary potential energy, the equilibrium condition becomes a functional stationary problem. Under the homogenization assumptions, the macroscopic potential energy is related via the volume averages of the microscopic ones and the entire potential energy is defined by

$$\Phi = \int_\Omega \frac{1}{|V|}\int_{Y_0} W dY dX - \int_{\partial\Omega} \mathbf{t} \cdot \mathbf{u} dS, \tag{9}$$

where $W$ is the strain energy function of the microstructure defined by the deformation gradient $\mathbf{F}$, and assuming conservative tractions. The stationary condition becomes

$$\delta\Phi = \int_\Omega \frac{1}{|V|}\int_{Y_0} \delta\mathbf{F} : \Pi dY dX - F_{ext}(\delta\mathbf{u}) = 0, \tag{10}$$

$$\Pi = \frac{\partial W}{\partial \mathbf{F}}, \tag{11}$$

$$F_{ext}(\delta\mathbf{u}) = \int_{\partial\Omega} \mathbf{t} \cdot \delta\mathbf{u} dS. \tag{12}$$

A similar equation has been reported by Terada and Kikuchi [5] using two-scale convergence theory [17]. We have also shown a formulation based on the mixed variational principle with a perturbed Lagrange-multiplier [14]. By inserting Eq. (6) into Eq. (10), macro and micro equilibrium equations can be derived based on the defined space of the variation.

$$\overline{G} = \int_\Omega \frac{1}{|V|}\int_{Y_0} \delta\overline{\mathbf{F}} : \Pi dY dX - F_{ext}(\delta\mathbf{u}) = 0, \tag{13}$$

$$G = \int_{Y_0} \delta\tilde{\mathbf{Z}} : \Pi dY = 0, \tag{14}$$

which achieves equilibrium under the given boundary condition in the macrostructure and self-equilibrium under a periodic boundary condition, Eq. (8), of the microscopic displacement in the microstructure. Thus the homogenization method simultaneously satisfies the two equilibrium conditions as described above. To solve the nonlinear equation, the Newton–Raphson method is employed. Then the standard linearization process in nonlinear finite element method provides the following linearized equations

$$\int_\Omega \frac{1}{|V|}\int_{Y_0} \delta\mathbf{F} : \mathbf{A} : \Delta\mathbf{F} dY dX = F_{ext}(\delta\mathbf{u}) - \int_\Omega \frac{1}{|V|}\int_{Y_0} \delta\mathbf{F} : \Pi dY dX, \tag{15}$$

$$\mathbf{A} = \frac{\partial \Pi}{\partial \mathbf{F}}. \tag{16}$$

Substituting Eqs. (5) and (6) into the above equation yields

$$\int_\Omega \frac{1}{|V|}\int_{Y_0} s(\delta\overline{\mathbf{F}} + \delta\tilde{\mathbf{Z}}) : \mathbf{A} : (\Delta\overline{\mathbf{F}} + \Delta\tilde{\mathbf{Z}}) dY dX = F_{ext}(\delta\mathbf{u}) - \int_\Omega \frac{1}{|V|}\int_{Y_0} (\delta\overline{\mathbf{F}} + \delta\tilde{\mathbf{Z}}) : \Pi dY dX. \tag{17}$$

By finite element discretization using

$$\Delta\overline{\mathbf{F}} = [\overline{B^e}]\{\Delta\mathbf{u}^e\}, \tag{18}$$

$$\Delta\tilde{\mathbf{Z}} = [B^e]\{\Delta\mathbf{w}^e\}, \tag{19}$$

where $[B^e]$ is a shape function matrix, the left-hand side of Eq. (17) becomes

$$\begin{aligned}
&\{\delta\mathbf{w}^Q\}\frac{1}{|V|}\int_{Y_0}[B^e]^T[A][B^e]dY\{\Delta\mathbf{w}^Q\}\\
&\quad+\{\delta\mathbf{w}^Q\}\frac{1}{|V|}\int_{Y_0}[B^e]^T[A]dY[\overline{B^e}]\{\Delta\mathbf{u}^e\}\\
&\quad+\{\delta\mathbf{u}^e\}[\overline{B^e}]^T\frac{1}{|V|}\int_{Y_0}[A][B^e]dY\{\Delta\mathbf{w}^Q\}\\
&\quad+\{\delta\mathbf{u}^e\}[\overline{B^e}]^T\frac{1}{|V|}\int_{Y_0}[A]dY[\overline{B^e}]\{\Delta\mathbf{u}^e\}\\
&=\{\delta\mathbf{w}^Q\}\mathbf{K}^Q_{ww}\{\Delta\mathbf{w}^Q\}+\{\delta\mathbf{w}^Q\}\mathbf{K}^Q_{wu}\{\Delta\mathbf{u}^e\}\\
&\quad+\{\delta\mathbf{u}^e\}\mathbf{K}^Q_{uw}\{\Delta\mathbf{w}^Q\}+\{\delta\mathbf{u}^e\}\mathbf{K}^Q_{uu}\{\Delta\mathbf{u}^e\},
\end{aligned}\tag{20}$$

while the second term of the right-hand side of Eq. (17) becomes

$$-\{\delta\mathbf{u}^e\}[\overline{B^e}]^T\frac{1}{|V|}\int_{Y_0}[\Pi]dY-\{\delta\mathbf{w}^Q\}\frac{1}{|V|}\int_{Y_0}[B^e]^T[\Pi]dY,\tag{21}$$

at each quadrature point of the macrostructure. Symbol $Q$ denotes the quantity that is evaluated at a macroscopic quadrature point, while symbol $e$ denotes the quantity evaluated in the macroscopic element. By assembling these appropriately on the macro continuum, and considering the facultative variations, the following semi-positive definite symmetric matrix is obtained

$$\begin{bmatrix}\mathbf{K}_{ww}&\mathbf{K}_{wu}\\ \mathbf{K}_{uw}&\mathbf{K}_{uu}\end{bmatrix}\begin{Bmatrix}\Delta\mathbf{w}\\ \Delta\mathbf{u}\end{Bmatrix}=\begin{Bmatrix}\mathbf{r}_w\\ \mathbf{r}_u\end{Bmatrix},\tag{22}$$

where

$$\mathbf{K}_{ww}=\int_\Omega\left(\frac{1}{|V|}\int_{Y_0}[B^e]^T[A][B^e]dY\right)dX\tag{23}$$

$$\mathbf{K}_{wu}=\int_\Omega\left(\frac{1}{|V|}\int_{Y_0}[B^e]^T[A]dY\right)[\overline{B^e}]dX\tag{24}$$

$$\mathbf{K}_{uw}=\int_\Omega[\overline{B^e}]^T\left(\frac{1}{|V|}\int_{Y_0}[A][B^e]dY\right)dX\tag{25}$$

$$\mathbf{K}_{uu}=\int_\Omega[\overline{B^e}]^T\left(\frac{1}{|V|}\int_{Y_0}[A]dY\right)[\overline{B^e}]dX\tag{26}$$

$$\{\mathbf{r}_w\}=-\int_\Omega\left(\frac{1}{|V|}\int_{Y_0}[B^e]^T[\Pi]dY\right)dX\tag{27}$$

$$\{\mathbf{r}_u\}=F_{ext}-\int_\Omega[\overline{B^e}]^T\left(\frac{1}{|V|}\int_{Y_0}[\Pi]dY\right)dX.\tag{28}$$

The nonlinear homogenization method solves Eq. (22) for $\Delta\mathbf{u}$ and $\Delta\mathbf{w}$ under the given boundary condition for the macrostructure and the periodic boundary condition (Eq. 8) for microscopic displacement. The number of degrees of freedom (NDOF) of this matrix is (NDOF of macrostructure + quadrature point of macrostructure × NDOF of microstructure). An enormous computational cost is, however, required to solve a small-scale problem. Moreover, it is difficult to solve the form given in Eq. (8) due to memory limitations, and generally, a transformation into the weak form takes place as described below.

### 2.3 Characteristic deformation

In a nonlinear problem, to evaluate the response of a microstructure to macroscopic deformation in a similar way to that in a linear problem [18], we obtain the following equation by taking the derivative of Eq. (14) at each quadrature point and substituting Eqs. (5) and (16).

$$\int_{Y_0}\delta\tilde{\mathbf{Z}}:\mathbf{A}:d\tilde{\mathbf{Z}}dY=-\int_{Y_0}\delta\tilde{\mathbf{Z}}:\mathbf{A}:d\overline{\mathbf{F}}dY\tag{29}$$

Since the macroscopic deformation gradient is independent of the microscopic integration,

$$\int_{Y_0}\delta\tilde{\mathbf{Z}}:\mathbf{A}:\frac{\partial\tilde{\mathbf{Z}}}{\partial\overline{\mathbf{F}}}dY=-\int_{Y_0}\delta\tilde{\mathbf{Z}}:\mathbf{A}:\mathbf{I}dY,\tag{30}$$

where $\mathbf{I}$ is a fourth order identity tensor, and the microstructural response of the macroscopic deformation gradient becomes

$$\frac{\partial\tilde{\mathbf{Z}}}{\partial\overline{\mathbf{F}}}=\nabla_Y\left(\frac{\partial\mathbf{w}}{\partial\overline{\mathbf{F}}}\right)\equiv-\nabla_Y\chi,\tag{31}$$

$$\chi\equiv-\frac{\partial\mathbf{w}}{\partial\overline{\mathbf{F}}},\tag{32}$$

where a third order tensor $\chi$ is the derivative of the microscopic displacement with respect to the macroscopic deformation gradient. This is referred to as the characteristic deformation for nonlinear problems. The equation above can be substituted into Eq. (30) yielding

$$\int_{Y_0}\delta\tilde{\mathbf{Z}}:\mathbf{A}:\nabla_Y\chi dY=\int_{Y_0}\delta\tilde{\mathbf{Z}}:\mathbf{A}:\mathbf{I}dY.\tag{33}$$

By finite element discretization, the gradient of $\chi$ becomes

$$\nabla_Y \chi = [B^e][\chi^e], \tag{34}$$

in a microscopic finite element. $[\chi^e]$ is the derivative of the microscopic displacement for each component of $\overline{\mathbf{F}}$; in other words, it is the matrix given below with nine kinds of characteristic deformation.

$$[\chi^e] = \begin{bmatrix} \chi^e_{111} & \chi^e_{112} & \cdots & \chi^e_{133} \\ \chi^e_{211} & \chi^e_{212} & \cdots & \chi^e_{233} \\ \vdots & \vdots & \ddots & \vdots \\ \chi^e_{n11} & \chi^e_{n12} & \cdots & \chi^e_{n33} \end{bmatrix}, \tag{35}$$

where $n$ is the NDOF of one finite element of the microstructure. The matrix equation becomes

$$\mathbf{K}_\chi [\chi^Q] = [\mathbf{r}_\chi], \tag{36}$$

$$\mathbf{K}_\chi = \int_{Y_0} [B^e]^T [A][B^e] dY, \tag{37}$$

$$[\mathbf{r}_\chi] = \int_{Y_0} [B^e]^T [A][I] dY, \tag{38}$$

from Eq. (33) about one microstructure. $[\chi^Q]$ denotes that the quantity is evaluated at the macroscopic quadrature point. The value of $[\chi^Q]$, which is a (NDOF of the microstructure) row $\times$ 9 column matrix, can be obtained by assembling $[\chi^e]$. $[I]$ is a ninth order identity matrix, consisting of nine column vectors $\{I_i\}(i = 1 \ldots 9)$. Thus nine solutions can be obtained for the right-hand side of Eq. (38), one for each $\{I_i\}$ corresponding to a component of the deformation gradient. $[\chi^Q]$ can then be obtained by solving each different version of the right-hand side of the above equation.

Multiplying by $[\overline{B^e}]$ and dividing by $|V|$ on both sides, Eq. (36) yields

$$\frac{1}{|V|}\mathbf{K}_\chi [\chi^Q][\overline{B^e}] = \frac{1}{|V|}[\mathbf{r}_\chi][\overline{B^e}]. \tag{39}$$

Now, by using Eq. (20)

$$\frac{1}{|V|}\mathbf{K}_\chi = \mathbf{K}^Q_{ww}, \tag{40}$$

$$\frac{1}{|V|}[\mathbf{r}_\chi][\overline{B^e}] = \mathbf{K}^Q_{wu}, \tag{41}$$

and thus,

$$\mathbf{K}^Q_{ww}[\chi^Q][\overline{B^e}] = \mathbf{K}^Q_{wu}. \tag{42}$$

The total is obtained at all macroscopic quadrature points in respect of the above equation

$$\mathbf{K}_{ww}[\chi][\overline{B}] = \mathbf{K}_{wu}, \tag{43}$$

$$[\overline{B}] \equiv \sum_i [\overline{B^e}], \tag{44}$$

$$[\chi] \equiv \sum_i [\chi^Q], \tag{45}$$

where $[\chi]$ is a matrix consisting of (quadrature points of macrostructure $\times$ NDOF of microstructure) rows $\times$ 9 columns.

The characteristic deformations are the deformation increments for unit macroscopic deformation gradients at a particular instant and these describe the material properties and strain distribution of the microstructure. Equation (29) can also be considered a linear approximation of the microscopic deformation. Therefore, the update of the microscopic deformation by

$$\Delta \mathbf{w} = -\chi : \Delta \overline{\mathbf{F}}, \tag{46}$$

corresponds to the Forward Euler method for microscopic deformation from Eq. (32).

### 2.4 Homogenization method using characteristic deformation mode superposition

In the mode superposition homogenization method, the microscopic displacement increment is approximately obtained by the linear combination of the previously calculated characteristic deformation ${}_0\chi$ and the scaling factor from Eq. (46) as in [10]

$$\Delta w_k \doteqdot -{}_0\chi_{kpQ} \Delta\alpha_{pQ}, \tag{47}$$

where $\alpha$ is the scaling factor for each mode. Inserting Eq. (47) into Eq. (22) yields the matrix

$$\begin{bmatrix} [{}_0\chi]^T & \mathbf{0} \\ \mathbf{0} & \mathbf{I} \end{bmatrix} \begin{bmatrix} \mathbf{K}_{ww} & \mathbf{K}_{wu} \\ \mathbf{K}_{uw} & \mathbf{K}_{uu} \end{bmatrix} \begin{bmatrix} [{}_0\chi] & \mathbf{0} \\ \mathbf{0} & \mathbf{I} \end{bmatrix} \begin{Bmatrix} \Delta\alpha \\ \Delta\mathbf{u} \end{Bmatrix} = \begin{bmatrix} [{}_0\chi]^T & \mathbf{0} \\ \mathbf{0} & \mathbf{I} \end{bmatrix} \begin{Bmatrix} \mathbf{r}_w \\ \mathbf{r}_u \end{Bmatrix} \tag{48}$$

$$\begin{bmatrix} [{}_0\chi]^T \mathbf{K}_{ww} [{}_0\chi] & [{}_0\chi]^T \mathbf{K}_{wu} \\ \mathbf{K}_{uw} [{}_0\chi] & \mathbf{K}_{uu} \end{bmatrix} \begin{Bmatrix} \Delta\alpha \\ \Delta\mathbf{u} \end{Bmatrix} = \begin{Bmatrix} [{}_0\chi]^T \mathbf{r}_w \\ \mathbf{r}_u \end{Bmatrix}, \tag{49}$$

where $[{}_0\chi]$ is the same kind of matrix as $[\chi]$. The above equation can be represented as

$$\begin{bmatrix} \mathbf{K}_{\alpha\alpha} & \mathbf{K}_{\alpha u} \\ \mathbf{K}_{u\alpha} & \mathbf{K}_{uu} \end{bmatrix} \begin{Bmatrix} \Delta\alpha \\ \Delta\mathbf{u} \end{Bmatrix} = \begin{Bmatrix} \mathbf{r}_\alpha \\ \mathbf{r}_u \end{Bmatrix}, \tag{50}$$

where

$$\mathbf{K}_{\alpha\alpha} = \int_{\Omega} \left( \frac{1}{|V|} \int_{Y_0} [{}_0\chi^e]^T [B^e]^T [A][B^e][{}_0\chi^e] dY \right) dX, \tag{51}$$

$$\mathbf{K}_{\alpha u} = -\int_{\Omega} \left( \frac{1}{|V|} \int_{Y_0} [{}_0\chi^e]^T [B^e]^T [A] dY \right) [\overline{B^e}] dX, \tag{52}$$

$$\mathbf{K}_{u\alpha} = -\int_{\Omega} [\overline{B^e}]^T \left( \frac{1}{|V|} \int_{Y_0} [A][B^e][{}_0\chi^e] dY \right) dX, \tag{53}$$

$$\mathbf{K}_{uu} = \int_{\Omega} [\overline{B^e}]^T \left( \frac{1}{|V|} \int_{Y_0} [A] dY \right) [\overline{B^e}] dX, \tag{54}$$

$$\{\mathbf{r}_u\} = F_{ext} - \int_{\Omega} [\overline{B^e}]^T \left( \frac{1}{|V|} \int_{Y_0} [\Pi] dY \right) dX, \tag{55}$$

$$\{\mathbf{r}_\alpha\} = \int_{\Omega} \left( \frac{1}{|V|} \int_{Y_0} [{}_0\chi^e]^T [B^e]^T [\Pi] dY \right) dX. \tag{56}$$

We obtain the matrix with unknowns $\Delta\alpha$ and $\Delta\mathbf{u}$. Because the NDOF of the matrix is reduced to (NDOF of macrostructure + quadrature point of macrostructure $\times$ 9), significant computational cost is saved.

This technique is, however, an approximate means of achieving equilibrium in a range of displacements representing linear combinations of $\chi_0$, as it is clear from Eq. (56) that $\chi_0$ has an effect on the equilibrium. In this way, to approximate the deformation in limited deformation patterns, an approximation error is created depending on the analysis case [15].

## 3 Algorithm for nonlinear homogenization method

### 3.1 Generalized algorithm

In Eq. (22), $\{\Delta w\}$ can be statically condensed at the element quadrature point level and becomes

$$\{\Delta\mathbf{w}\} = \mathbf{K}_{ww}^{-1}(\{\mathbf{r}_w\} - \mathbf{K}_{wu}\{\Delta\mathbf{u}\}). \tag{57}$$

$\{\Delta w\}$ vanishes when the above equation is substituted in the macroscopic equilibrium equation

$$(\mathbf{K}_{uu} - \mathbf{K}_{uw}\mathbf{K}_{ww}^{-1}\mathbf{K}_{wu})\{\Delta\mathbf{u}\} = \{\mathbf{r}_u\} - \mathbf{K}_{uw}\mathbf{K}_{ww}^{-1}\{\mathbf{r}_w\}. \tag{58}$$

Now, the microscopic equilibrium hypothesized for $\overline{\mathbf{F}}$ at this time is

$$\{\mathbf{r}_w\} = 0. \tag{59}$$

By using Eqs. (43) and (57), we obtain [5]

$$\{\Delta\mathbf{w}\} = -\mathbf{K}_{ww}^{-1}\mathbf{K}_{wu}\{\Delta\mathbf{u}\} = -[\chi][\overline{\mathbf{B}}]\{\Delta\mathbf{u}\}. \tag{60}$$

By using Eqs. (43), (57), and (58) we can represent

$$(\mathbf{K}_{uu} - \mathbf{K}_{uw}[\chi][\overline{\mathbf{B}}])\{\Delta\mathbf{u}\} = \{\mathbf{r}_u\}, \tag{61}$$

where $(\mathbf{K}_{uu} - \mathbf{K}_{uw}[\chi][\overline{\mathbf{B}}])$ is called the homogenized tangent stiffness.

In differential equation form, from Eqs. (14), (17), and (31), this becomes

$$\int_{\Omega} \delta\overline{\mathbf{F}} : \left( \frac{1}{|V|} \int_{Y_0} \left( \mathbf{A} : (\mathbf{I} - \nabla_Y \chi) \right) dY \right) : \Delta\overline{\mathbf{F}} dX = \overline{\mathbf{F}}_{ext} - \int_{\Omega} \delta\overline{\mathbf{F}} : \left( \frac{1}{|V|} \int_{Y_0} \Pi dY \right) dX. \tag{62}$$

Microscopic equilibrium, Eq. (59),

$$r_w = \int_{Y_0} \delta\tilde{\mathbf{Z}} : \Pi dY = \mathbf{0}, \tag{63}$$

is a prerequisite of the above equation. To satisfy this nonlinear prerequisite, a Newton–Raphson iteration is needed. Thus the above equation is linearized with respect to $\mathbf{w}$ while $\overline{\mathbf{F}}$ is fixed, and then discretized by the finite element method using Eq. (19). At each quadrature point, the linearized self-equilibrated equation becomes

$$\int_{Y_0} [B^e]^T [A][B^e] dY \{\Delta\mathbf{w}^Q\} = -\int_{Y_0} [B^e]^T [\Pi] dY. \tag{64}$$

In the generalized algorithm, it is necessary to compute three different calculations in each iteration.

1. Update macroscopic tangential homogenization $\chi$ using Eq. (36).
2. Solve microscopic equilibrium problem, Eq. (63), and obtain the convergence solution $\{\mathbf{w}\}$ while $\overline{\mathbf{F}}$ is fixed.
3. Solve the linearized macroscopic equilibrium equation, Eq. (61), to obtain $\{\mathbf{u}\}$.

Processes 1 and 2 need to be solved at all quadrature points of the macrostructure and it is known that this contributes the most to the calculation load [6]. These processes require prohibitive computational cost and actual numerical simulation is difficult.

### 3.2 Block LU factorization algorithm

We now present an algorithm that decreases the residual of each scale simultaneously using the block LU factorization

algorithm without microscopic convergence in the macroscopic iteration as in the conventional algorithm. By block LU factorization, Eq. (22) becomes

$$\begin{bmatrix} \mathbf{K}_{ww} & \mathbf{0} \\ \mathbf{K}_{uw} & \mathbf{S} \end{bmatrix} \begin{bmatrix} \mathbf{I} & \mathbf{K}_{ww}^{-1}\mathbf{K}_{wu} \\ \mathbf{0} & \mathbf{I} \end{bmatrix} \begin{Bmatrix} \Delta\mathbf{w} \\ \Delta\mathbf{u} \end{Bmatrix} = \begin{Bmatrix} \mathbf{r}_w \\ \mathbf{r}_u \end{Bmatrix}, \tag{65}$$

where $\mathbf{S}$ is called the Schur-Complement. Referring to Eq. (43),

$$\begin{aligned} \mathbf{S} &= \mathbf{K}_{uu} - \mathbf{K}_{uw}\mathbf{K}_{ww}^{-1}\mathbf{K}_{wu} \\ &= \mathbf{K}_{uu} - \mathbf{K}_{uw}[\chi][\overline{\mathbf{B}}] \\ &= \mathbf{K}_{uu} - [\overline{\mathbf{B}}]^T[\chi]^T\mathbf{K}_{ww}[\chi][\overline{\mathbf{B}}], \end{aligned} \tag{66}$$

which corresponds to the homogenized tangent stiffness of Eq. (61). The solution process for Eq. (65) is composed of the forward substitution

$$\begin{bmatrix} \mathbf{K}_{ww} & \mathbf{0} \\ \mathbf{K}_{uw} & \mathbf{S} \end{bmatrix} \begin{Bmatrix} \Delta\tilde{\mathbf{w}} \\ \Delta\tilde{\mathbf{u}} \end{Bmatrix} = \begin{Bmatrix} \mathbf{r}_w \\ \mathbf{r}_u \end{Bmatrix}, \tag{67}$$

and the backward substitution

$$\begin{Bmatrix} \Delta\tilde{\mathbf{w}} \\ \Delta\tilde{\mathbf{u}} \end{Bmatrix} = \begin{bmatrix} \mathbf{I} & \mathbf{K}_{ww}^{-1}\mathbf{K}_{wu} \\ \mathbf{0} & \mathbf{I} \end{bmatrix} \begin{Bmatrix} \Delta\mathbf{w} \\ \Delta\mathbf{u} \end{Bmatrix}. \tag{68}$$

Then, from Eqs. (43), (67), and (68),

$$\mathbf{K}_{ww}\{\Delta\tilde{\mathbf{w}}\} = \{\mathbf{r}_w\}, \tag{69}$$

$$\mathbf{S}\{\Delta\mathbf{u}\} = \{\mathbf{r}_u\} - \mathbf{K}_{uw}\{\Delta\tilde{\mathbf{w}}\}, \tag{70}$$

$$\begin{aligned} \{\Delta\mathbf{w}\} &= \{\Delta\tilde{\mathbf{w}}\} - \mathbf{K}_{ww}^{-1}\mathbf{K}_{wu}\{\Delta\mathbf{u}\} \\ &= \{\Delta\tilde{\mathbf{w}}\} - [\chi]\Delta\overline{\mathbf{F}}, \end{aligned} \tag{71}$$

hold. The calculation process is described below.

1. Solve linearized microscopic equilibrium equation, Eq. (69), to obtain $\{\Delta\mathbf{w}\}$.
2. Solve linearized macroscopic equilibrium equation, Eq. (70), to obtain $\{\Delta\mathbf{u}\}$. Note that this equation is equivalent to Eq. (58).
3. Update $\{\Delta\mathbf{w}\}$ using Eq. (71). We have already obtained $[\chi]$ from the calculation of $\mathbf{S}$.

Three matrices, namely the micro, macro, and Schur-Complement, need to be solved at each iteration. Although the computational cost of this algorithm is expected to be lower than that of the generalized algorithm since equilibrium of the microstructure is not required at every iteration, the Schur-Complement update is still relatively expensive as described above. A similar algorithm for a differential equation using the Block-Newton method has been proposed by Yamada and Matsui [19].

### 3.3 Approximation of schur-complement in micro–macro coupled equation

In the block LU factorization algorithm described in the previous subsection, the linearized equations for the microstructure are solved first and then the increment for the macro-displacements is solved using the Schur-Complement that reflects the micro–macro interactions. These two steps essentially define the computational cost because the third step can be solved efficiently by reusing the characteristic deformation that has already been computed in the evaluation of the Schur-Complement in the second step. Although the macroscopic equilibrium conditions must be satisfied as well as the microscopic ones by making a convergence judgment for the residuals, the Schur-Complement is a tangent stiffness for prediction and does not influence the equilibrium directly. Hence, one of the requirements for efficient nonlinear homogenization algorithms is to approximate the Schur-Complement effectively. In this regard, we propose the two algorithms given below.

A simple method is to approximate the Schur-Complement using the previously calculated characteristic deformation ${}_0\chi$ as in

$$\begin{aligned} \mathbf{S} &= \mathbf{K}_{uu} - \mathbf{K}_{uw}[\chi][\overline{\mathbf{B}}] \\ &\doteqdot \mathbf{K}_{uu} - \mathbf{K}_{uw}[{}_0\chi][\overline{\mathbf{B}}] \\ &= \mathbf{K}_{uu} - [\overline{\mathbf{B}}]^T[\chi]^T\mathbf{K}_{ww}[{}_0\chi][\overline{\mathbf{B}}], \end{aligned} \tag{72}$$

that is,

$$[\chi]^T\mathbf{K}_{ww}[\chi] \doteqdot [\chi]^T\mathbf{K}_{ww}[{}_0\chi], \tag{73}$$

is employed from Eq. (66). Henceforth, this method is referred to as the modified block LU factorization algorithm (MBFA). The other approach is to make use of the aforementioned Mode Superposition method in the approximation of the Schur-Complement. The calculation process and an interpretation thereof are given below.

1. Solve the linearized microscopic equilibrium equation, Eq. (69), to obtain $\{\Delta\tilde{\mathbf{w}}\}$.
2. From Eq. (50), solve the mode superposition-based linearized micro–macro coupled equation

$$\begin{bmatrix} \mathbf{K}_{\alpha\alpha} & \mathbf{K}_{\alpha u} \\ \mathbf{K}_{u\alpha} & \mathbf{K}_{uu} \end{bmatrix} \begin{Bmatrix} \Delta\alpha \\ \Delta\mathbf{u} \end{Bmatrix} = \begin{Bmatrix} \mathbf{r}_\alpha \\ \mathbf{r}_u \end{Bmatrix}, \tag{74}$$

   to obtain $\{\Delta\mathbf{u}\}$. Then, $\mathbf{S}$ is approximated by the range of the mode superposition method and the update of $\mathbf{S}$ can be omitted.
3. The assumption of the mode superposition method follows from Eqs. (46), (47), and (71), and $\{\Delta\mathbf{w}\}$ is updated using

$$\{\Delta \mathbf{w}\} = \{\Delta \tilde{\mathbf{w}}\} - [_0\chi]\{\Delta\alpha\}. \tag{75}$$

The meaning of the algorithm is now given. Block LU factorization is applied to Eq. (74) yielding

$$\mathbf{K}_{\alpha\alpha}\{\Delta\tilde{\alpha}\} = \{\mathbf{r}_\alpha\}, \tag{76}$$

$$(\mathbf{K}_{uu} - \mathbf{K}_{u\alpha}\mathbf{K}_{\alpha\alpha}^{-1}\mathbf{K}_{\alpha u})\{\Delta\mathbf{u}\} = \{\mathbf{r}_u\} - \mathbf{K}_{u\alpha}\{\Delta\tilde{\alpha}\}, \tag{77}$$

$$\{\Delta\alpha\} = \{\Delta\tilde{\alpha}\} - \mathbf{K}_{\alpha\alpha}^{-1}\mathbf{K}_{\alpha u}\{\Delta\mathbf{u}\}. \tag{78}$$

In Eq. (77), the macroscopic displacement is updated using

$$(\mathbf{K}_{uu} - \mathbf{K}_{u\alpha}\mathbf{K}_{\alpha\alpha}^{-1}\mathbf{K}_{\alpha u}), \tag{79}$$

which can be considered an approximation of the homogenized tangent stiffness. Then, using Eqs. (43) and (66), the Schur-Complement becomes

$$\begin{aligned}
\mathbf{S} &= \mathbf{K}_{uu} - \mathbf{K}_{uw}[\chi][\overline{\mathbf{B}}] \\
&= \mathbf{K}_{uu} - \mathbf{K}_{uw}[\chi]([\chi]^T\mathbf{K}_{ww}[\chi])^{-1}([\chi]^T\mathbf{K}_{ww}[\chi])[\overline{\mathbf{B}}] \\
&= \mathbf{K}_{uu} - \mathbf{K}_{uw}[\chi]([\chi]^T\mathbf{K}_{ww}[\chi])^{-1}[\chi]^T\mathbf{K}_{wu} \\
&\doteqdot \mathbf{K}_{uu} - \mathbf{K}_{uw}[_0\chi]([_0\chi]^T\mathbf{K}_{ww}[_0\chi])^{-1}[_0\chi]^T\mathbf{K}_{wu} \\
&= \mathbf{K}_{uu} - [\overline{\mathbf{B}}]^T[\chi]^T\mathbf{K}_{ww}[_0\chi] \\
&\quad \times([_0\chi]^T\mathbf{K}_{ww}[_0\chi])^{-1}[_0\chi]^T\mathbf{K}_{ww}[\chi][\overline{\mathbf{B}}] \\
&= \mathbf{K}_{uu} - \mathbf{K}_{u\alpha}\mathbf{K}_{\alpha\alpha}^{-1}\mathbf{K}_{\alpha u},
\end{aligned} \tag{80}$$

that is,

$$\begin{aligned}
&[\chi]^T\mathbf{K}_{ww}[\chi] \doteqdot [\chi]^T\mathbf{K}_{ww}[_0\chi] \\
&\quad \times([_0\chi]^T\mathbf{K}_{ww}[_0\chi])^{-1}[_0\chi]^T\mathbf{K}_{ww}[\chi],
\end{aligned} \tag{81}$$

is employed. In the mode superposition method, since the homogenized tangent stiffness corresponds to the exact value with the mode updated at every Newton–Raphson iteration as described above, this method can give an approximate mean of the homogenized tangent stiffness by decreasing the number of times that the mode is updated. This method is referred to as the mode superposition algorithm (MSA).

## 4 Numerical examples

### 4.1 Comparison of computational costs and convergence properties

With respect to computational cost and convergence, which are of interest to us, we now compare the four methods introduced in the previous section, namely, the generalized algorithm (GA), block LU factorization algorithm (BFA), modified block LU factorization algorithm (MBFA) and the algorithm using mode superposition (MSA). Detailed algorithms for the parallel computation of each of the methods are given in Fig. 2. The GA calculates the microscopic equilibrium at each quadrature point in every iteration. In contrast to the GA, the BFA, MBFA, and MSA decrease the residual

1. Set calculation condition
2. Perform in a unit cell at each quadrature point by paraell computation
   Solve microscopic equilibrium problem : $\{\mathbf{r}_w\} = 0$
   Update the microscopic deformation : $\{\mathbf{w}\}$
   Solve for update $\chi$ : $\mathbf{K}_\chi[\chi^Q] = [\mathbf{r}_\chi]$
   Compute : $\mathbf{K}_{uu} - \mathbf{K}_{uw}\mathbf{K}_{ww}^{-1}\mathbf{K}_{wu}, \{\mathbf{r}_u\}$
3. Communication using MPIallreduce
   Assemble : $\mathbf{K}_{uu} - \mathbf{K}_{uw}\mathbf{K}_{ww}^{-1}\mathbf{K}_{wu}, \{\mathbf{r}_u\}$
4. Solve
   $$(\mathbf{K}_{uu} - \mathbf{K}_{uw}[\chi][\overline{\mathbf{B}}])\{\Delta\mathbf{u}\} = \{\mathbf{r}_u\}$$
5. Update the vatiables
   $$\{\mathbf{u}\} = \{\mathbf{u}\} + \{\Delta\mathbf{u}\}$$
6. if $|\{\mathbf{r}_u\}| < Tol$, then
   Next step GOTO 1
   else
   Next iteration GOTO 2

**(a)**

1. Set calculation condition
2. Perform in a unit cell at each quadrature point by paraell computation
   Compute : $\mathbf{K}_{ww}, \{\mathbf{r}_w\}$
   Solve : $\mathbf{K}_{ww}\{\Delta\tilde{\mathbf{w}}\} = \{\mathbf{r}_w\}$
   Update the microscopic deformation: $\{\mathbf{w}\} = \{\mathbf{w}\} + \{\Delta\tilde{\mathbf{w}}\}$
   In the BFA, everytime solve for update $\chi$ : $\mathbf{K}_\chi[\chi^Q] = [\mathbf{r}_\chi]$
   ( In the MBFA, sometime solve for update $\chi_0$ : $\mathbf{K}_\chi[\chi^Q] = [\mathbf{r}_\chi]$ )
   Compute : $\mathbf{S}, \{\mathbf{r}_u\} - \mathbf{K}_{uw}\{\Delta\tilde{\mathbf{w}}\}$
3. Communication using MPIallreduce
   Assemble : $\mathbf{S}, \{\mathbf{r}_u\} - \mathbf{K}_{uw}\{\Delta\tilde{\mathbf{w}}\}$
4. Solve
   $$\mathbf{S}\{\Delta\mathbf{u}\} = \{\mathbf{r}_u\} - \mathbf{K}_{uw}\{\Delta\tilde{\mathbf{w}}\}$$
5. Update the vatiables
   $\{\mathbf{u}\} = \{\mathbf{u}\} + \{\Delta\mathbf{u}\}$
   In the BFA, $\{\mathbf{w}\} = \{\tilde{\mathbf{w}}\} - [\chi]\Delta\overline{\mathbf{F}}$
   In the MBFA, $\{\mathbf{w}\} = \{\tilde{\mathbf{w}}\} - [_0\chi]\Delta\overline{\mathbf{F}}$
6. if $|\{\mathbf{r}_w\}| < Tol, |\{\mathbf{r}_u\}| < Tol$, then
   Next step GOTO 1
   else
   Next iteration GOTO 2

**(b)**

1. Set calculation condition
2. Perform in a unit cell at each quadrature point by paraell computation
   Compute : $\mathbf{K}_{ww}, \{\mathbf{r}_w\}$
   Solve : $\mathbf{K}_{ww}\{\Delta\tilde{\mathbf{w}}\} = \{\mathbf{r}_w\}$
   Update the microscopic deformation: $\{\mathbf{w}\} = \{\mathbf{w}\} + \{\Delta\tilde{\mathbf{w}}\}$
   ( Sometime solve for update $\chi_0$ : $\mathbf{K}_\chi[\chi^Q] = [\mathbf{r}_\chi]$ )
   Compute : $\mathbf{K}_{uu}, \mathbf{K}_{u\alpha}, \mathbf{K}_{\alpha u}, \mathbf{K}_{\alpha\alpha}, \{\mathbf{r}_\alpha\}, \{\mathbf{r}_u\}$
3. Communication using MPIallreduce
   Assemble : $\mathbf{K}_{uu}, \mathbf{K}_{u\alpha}, \mathbf{K}_{\alpha u}, \mathbf{K}_{\alpha\alpha}, \{\mathbf{r}_\alpha\}, \{\mathbf{r}_u\}$
4. Solve
   $$\begin{bmatrix} \mathbf{K}_{\alpha\alpha} & \mathbf{K}_{\alpha u} \\ \mathbf{K}_{u\alpha} & \mathbf{K}_{uu} \end{bmatrix} \begin{Bmatrix} \Delta\alpha \\ \Delta\mathbf{u} \end{Bmatrix} = \begin{Bmatrix} \mathbf{r}_\alpha \\ \mathbf{r}_u \end{Bmatrix}$$
5. Update the vatiables
   $$\{\mathbf{u}\} = \{\mathbf{u}\} + \{\Delta\mathbf{u}\}$$
   $$\{\alpha\} = \{\alpha\} + \{\Delta\alpha\}$$
   $$\{\mathbf{w}\} = \{\tilde{\mathbf{w}}\} - [_0\chi]\{\Delta\alpha\}$$
6. if $|\{\mathbf{r}_w\}| < Tol, |\{\mathbf{r}_u\}| < Tol$, then
   Next step GOTO 1
   else
   Next iteration GOTO 2

**(c)**

**Fig. 2** Algorithms for parallel computation using the message passing interface (MPI). **a** Algorithms for GA. **b** Algorithms for BFA and MBFA. **c** Algorithms for MSA

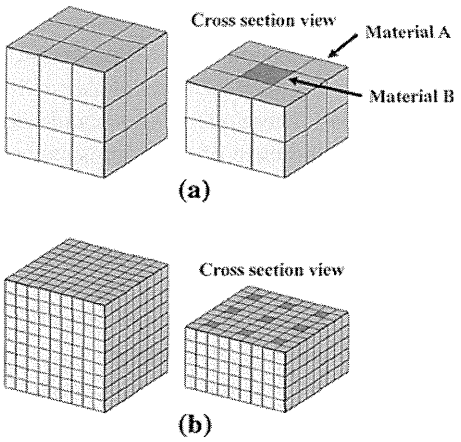


**Fig. 3** FE models used in the calculation time evaluation. **a** 64 nodes, 27 elements (minimum size). **b** 1000 nodes, 729 elements

**Table 1** Material constants for the models used in the calculation time evaluation

| | $E$[kPa] | $\nu$ |
|---|---|---|
| Material A in Fig. 3 | 0.1 | 0.3 |
| Material B in Fig. 3 | 10.0 | 0.3 |

of both scales simultaneously. Moreover, in the MBFA and MSA the straightforward update of S is avoided. We performed a 20% tensile test using the mesh of the block shown in Fig. 3 as the microstructure, and a single 8-node element as the macrostructure. The minimum size of the mesh is constructed from 27 ($3 \times 3 \times 3$) elements as shown in Fig. 3a, with the stiffness of the center element different from the rest.

The NDOF is adjusted by adding the same number of minimum units in each direction (e.g. Fig. 3b). The St. Venant hyperelastic material is used for the constitutive equations

$$W = \frac{1}{2}\lambda(tr\mathbf{E})^2 + \mu\mathbf{E} : \mathbf{E}, \tag{82}$$

$$\mathbf{S} = \frac{\partial W}{\partial \mathbf{E}} = (\lambda\mathbf{I} \otimes \mathbf{I} + 2\mu\mathbf{I}) : \mathbf{E} = \mathbf{C} : \mathbf{E}, \tag{83}$$

$$l_{ijkl} = \delta_{ik}\delta_{jl}, \tag{84}$$

$$\lambda = \frac{E\nu}{(1+\nu)(1-2\nu)}, \quad \mu = G = \frac{E}{2(1+\nu)}, \tag{85}$$

where $\mathbf{I}$ is a second order identity tensor, $\lambda$ and $\mu$ are Lame constants, and $E$ and $\nu$ are, respectively, Young's modulus and Poisson's ratio. $\mathbf{C}$ is a fourth order constant elasticity tensor and the relationship between $\boldsymbol{S}$ and $\boldsymbol{E}$ is linear. The material constants are given in Table 1. If the material constants are assumed to be uniform in the microstructure, the solutions obtained by these methods agree completely with the theoretical solution in the case of infinitesimal deformation. We have thus confirmed the correctness of the formulations

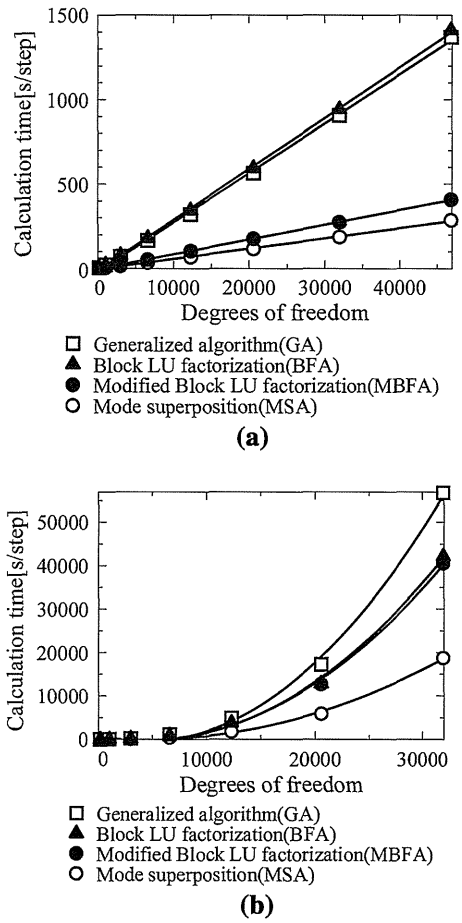


**Fig. 4** Comparison of calculation time. **a** Iterative solver. **b** Direct solver

and computer programs. The relationship between calculation time and NDOF of the microstructure for each algorithm is depicted in Fig. 4 for cases where an iterative solver (ILU preconditioned GMRES method) or direct solver (skyline method) are used. The breakdown of calculation time and number of iterations in each process, where the NDOF of the microstructure is 31,944, are given in Table 2. Convergence is judged to occur when the root sum square reaches $1 \times 10^{-10}$ times the initial value. As shown in Fig. 4, the calculation time of the BFA using an iterative solver slightly exceeds that of the GA. In the BFA, equilibrium of the microstructure is not required within an iteration for the sake of computational efficiency, but this may result in more iterations compared with the GA. Table 2 illustrates this, in that the BFA requires 5 iterations whereas the GA requires 4. We need to calculate the characteristic deformation to update the Schur-Complement; this means that the nine different right-hand sides of Eq. (33) must be solved in the case of the iterative solver. Consequently, the increased number of iterations results in a deterioration in the performance of the BFA. If a direct solver is used instead, the result of the LU decomposition

**Table 2** Calculation time and number of iterations in each process

| | Calculation of $\chi$ (s) | Calculation of equilibrium in the microscopic model (s) | Total (s) | No. of iterations |
|---|---|---|---|---|
| a. Iterative solver | | | | |
| GA | 670 | 211 | 906 | 4 |
| BFA | 805 | 107 | 942 | 5 |
| MBFA | 17 | 195 | 273 | 11 |
| MSA | 21 | 113 | 186 | 5 |
| b. Direct solver | | | | |
| GA | 19,816 | 36,949 | 56,791 | 4 |
| BFA | 23,689 | 18,492 | 42,212 | 5 |
| MBFA | 451 | 40,050 | 40,557 | 11 |
| MSA | 457 | 18,237 | 18,746 | 5 |

of the stiffness matrix can be reused in the computation of the characteristic deformation, and as a result, the computational cost of the BFA is 20% less than that of the GA, despite the BFA using one more iteration than the GA. On the other hand, the MBFA is much faster than both the BFA and the GA when an iterative solver is used, although in the case of a direct solver there is almost no difference between the MBFA and BFA. This is because the calculation cost of the mode update in the BFA is similar to that of the increased iterations in the MBFA. However, convergence in the MBFA is slow as shown in Fig. 5 and it is anticipated that for strong nonlinear problems, convergence may not be achieved at all. Here, the characteristic deformation was approximated by that obtained at the beginning of the analysis. Convergence can be improved by incorporating more frequent updates, at the expense of CPU time. Compared with these methods, the MSA always exhibits excellent speed and convergence. The advantage of the MSA is twofold. First, the approximation of the Schur-Complement is more accurate than in the MBFA, i.e., Eq. (80) gives a superior approximation than Eq. (72). Second, in an iteration of the MSA, the microscopic equation is solved in Eq. (75) in terms of $\Delta\alpha$ as well as in Eq. (74) with Eq. (69). These advantages should contribute to an accelerated convergence of the microscopic equation as well as the macroscopic equation. Although the St. Venant hyperelastic material assumed here has relatively weak nonlinearity, the number of iterations does not increase up to a large deformation range, even with the initial characteristic deformation being used for ${}_0\chi$. However, a periodic update of ${}_0\chi$ is required in the case of strong nonlinear material, such as an elasto-plastic material. If ${}_0\chi$ is updated at every iteration, the homogenized tangent stiffness corresponds to the exact value as described in Eq. (80).

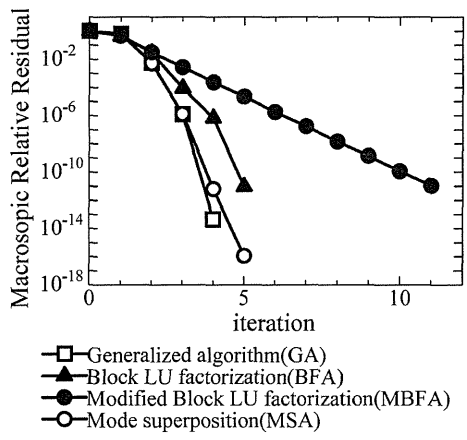


**Fig. 5** Comparison of convergence property

## 4.2 Application to ventricle–cardiomyocyte analysis with parallel computation

As seen in Table 2, most of the calculation cost relates to the microscopic equilibrium (Eq. (69)) when the MBFA or MSA is used. In addition, as the NDOF of the microscopic model becomes larger, the computational cost for the macroscopic model becomes more negligible. It is therefore crucial to decrease the time for microscopic calculation in real problems. Since Eq. (69) holds independently at each macroscopic quadrature point, parallel computation is effective in the homogenization method. In other words, microscopic models can be distributed equally to the available cores, and this directly accelerates the microscopic calculation according to the number of cores. Moreover, since the memory is shared by fewer microscopic models in the parallel computation, a greater NDOF of the microstructure can be handled.

Figures 6 and 7 show a simplified human cardiomyocyte–ventricle model, to which we have applied the MSA. As shown on the left and in the center of Fig. 7 a simplified cardiomyocyte model is constructed with extracellular and intracellular matrices and gap junctions. The total NDOF is 20385. If the models are arrayed periodically in the three directions as depicted on the right of the figure, a fairly accurate imitation of a microgram of real tissue is obtained. The

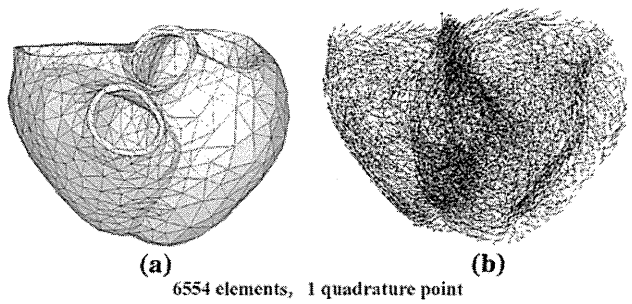


**Fig. 6** FE meshes of ventricles as macroscopic model. **a** FE mesh. **b** Fiber orientation

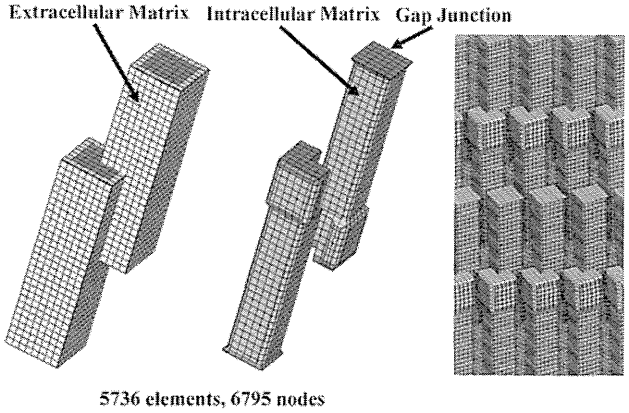


**Fig. 7** FE meshes of cardiomyocytes as microscopic model

**Table 3** Material constants for the cell model

| | $C_1$ | $C_2$ | $\kappa$ |
|---|---|---|---|
| Gap Junction | $1 \times 10^5$ | $1 \times 10^5$ | $2 \times 10^5$ |
| Intracellular Matrix | $1 \times 10^4$ | $1 \times 10^4$ | $2 \times 10^4$ |
| Extracellular Matrix | $1 \times 10^3$ | $1 \times 10^3$ | $2 \times 10^3$ |

Mooney–Rivlin material using reduced invariants is adopted for the constitutive equation, with the material constants listed in Table 3.

$$W = C_1(\tilde{I}_c - 3) + C_2(\tilde{II}_c - 3) + \frac{\kappa}{2}U^2 \tag{86}$$

$$\tilde{I}_c = \frac{I_c}{III_c^{1/3}}, \quad \tilde{II}_c = \frac{II_c}{III_c^{2/3}} \tag{87}$$

$$U = J - 1, \tag{88}$$

where $U$ is the volumetric strain energy function and $\kappa$ is the bulk modulus. The ventricle model is constructed based on CT imaging, with fiber directions distributed from $-90$ to 60 degrees, relative to the plane perpendicular to the long axis of the ventricle. The fiber direction denotes the long axis (z-axis) of the cardiomyocyte model, and therefore, proper rotation is taken into consideration for each micromodel. In this model, the intracellular matrix is defined as a function of a parameter that represents the excitation of the myocyte, and this parameter is varied at every time step to represent the transient contraction force. The homogenization method is applied to 6,554 elements covering the greater region of the ventricle, whereas the conventional Mooney–Rivlin hyperelastic constitutive law is assumed for the limited regions at the base and apex. To reduce the computational cost, a single myocyte (micromodel) is assigned to each finite element of the ventricle, i.e., 6,554 cardiomyocyte models are embedded in the ventricle model. The total NDOF, including those of the ventricles, amounts to 133,609,263.

The computer used was an IBM Blade Center consisting of 336 Power6 (4.0 GHz) processors. Considering the size of the problem, convergence was deemed to occur when the root sum square of the macro and micro residuals was $1 \times 10^{-5}$ times less than the initial value. Figure 8 shows the maximum, the minimum and the mean Green–Lagrange strains throughout the ventricle model, and the number of iterations of the MSA at each time step. The strains are measured in the fiber direction. Although the maximum and the minimum strains reach $\pm 20\%$, an excellent convergence property was observed. Figure 9 shows the resulting scalability, by depicting the speed up rate relative to a hundred-core computation. As shown in this figure, satisfactory parallel performance was obtained by the proposed algorithm. The deformations of the ventricle and a representative myocyte in the diastole and the systole are exemplified in Fig. 10. The CPU time for the completion of a cardiac cycle was about 24 h when using 300 cores. The proposed method thus allows us to deal with large-scale problems.

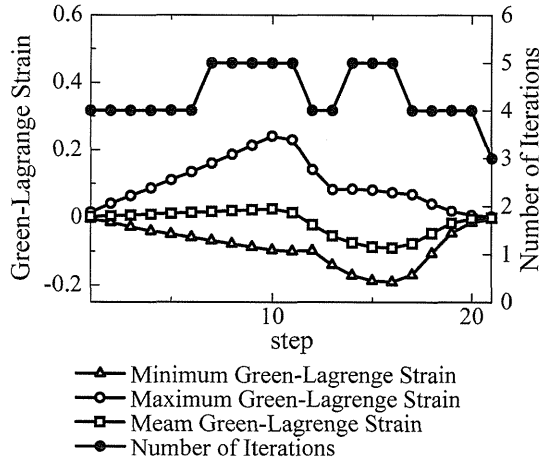


**Fig. 8** Green–Lagrenge strains and nunber of iterations at each step

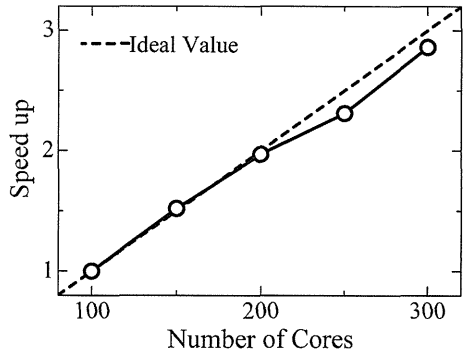


**Fig. 9** Speed up in parallel computation

## 5 Conclusion

To reduce the computational cost of the nonlinear homogenization method, the theoretical framework was reassessed

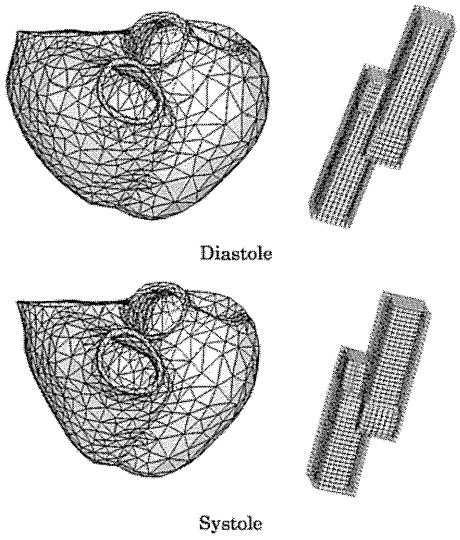


**Fig. 10** Deformations of macro and microstructures in diastole and systole

from the perspective of block LU factorization of the micro–macro coupled equation. Based on the relation between the characteristic deformation and the Schur-Complement as the homogenized tangent stiffness, a couple of approximation methods were introduced, namely, a simple scheme to reuse the old characteristic deformation (MBFA) and a sophisticated method based on the mode-superposition method (MSA) developed by our group. It is noted that accuracy is preserved in these approximation methods by incorporating the equilibrium conditions in both scales. Then, using a simplified FE model, the conventional algorithm (GA), a relative algorithm originating from the block LU factorization (BFA), the MBFA, and the MSA were compared and discussed. Of these methods, the MSA was found to be the best. Then, using the MSA, a large-scale human ventricle–cardiomyocyte simulation was performed on an IBM Blade Center consisting of 336 Power6 processors, and good parallel performance was demonstrated. We plan to use the proposed homogenization algorithm in a whole-heart simulation on a massively parallel computer in the near future.

**Acknowledgments** Our current research on homogenization method stems from Reference [10] coauthored by Hirohisa Noguchi. We again recognize his enthusiasm and contribution in a broad range of computational mechanics. This work was supported by Core Research for Evolutional Science and Technology, Japan Science and Technology Agency.



## References

1. Terada K, Hori M, Kyoya T, Kikuchi N (2000) Simulation of the multi-scale convergence in computational homogenization approaches. Int J Solids Struct 37:2285–2311
2. Hollister SJ, Kikuchi N (1992) Comparison of homogenization and standard mechanics analyses for periodic porous composites. Comput Mech 10:73–95
3. Breuls RGM, Sengers BG, Oomens CWJ, Bouten CVC, Baaijens FPT (2002) Predicting local cell deformations in engineered tissue constructs: a multilevel finite element approach. ASME J Biomech Eng 124:198–207
4. Krassowska W, Pilkington TC, Ideker RE (1990) Potential distribution in three-dimensional periodic myocardium: Part I. Solution with two-scale asymptotic analysis. IEEE Trans Biomed Eng 37:252–266
5. Terada K, Kikuchi N (2001) A class of general algorithms for multi-scale analyses of heterogeneous media. Comput Methods Appl Mech Eng 190:5427–5464
6. Matsui K, Terada K, Yuge K (2004) Two-scale finite element analysis of heterogeneous solids with periodic microstructures. Comput Struct 82:593–606
7. Takano N, Ohnishi Y, Zako M, Nishiyabu K (2001) Microstructure-based deep-drawing simulation of knitted fabric reinforced thermoplastics by homogenization theory. Int J Solids Struct 38:6333–6356
8. Rohan E (2003) Sensitivity strategies in modelling heterogeneous media undergoing finite deformation. Math Comput Simul 61:261–270
9. Moulinec H, Suquet P (1998) A numerical method for computing the overall response of nonlinear composites with complex microstructure. Comput Methods Appl Mech Eng 157:69–94
10. Yamamoto M, Hisada T, Noguchi H (2001) Homogenization method for large deformation problem by using characteristic deformation mode superposition. Trans Jpn Soc Mech Eng 67:1877–1884 (in Japanese)
11. Yamamoto M, Hisada T (2002) A homogenization method for nearly incompressible materials by using characteristic deformation mode superposition. Trans Jpn Soc Mech Eng A 45:596–602
12. Okada J, Hisada T (2006) Homogenization method for mixed finite element analysis of incompressible hyper-elastic materials. In: JSCES e06: Proceedings of the 11th computational engineering conference, Osaka, Japan, pp 79–82 (in Japanese)
13. Okada J, Hisada T (2006) Homogenization method for mixed finite element analysis of incompressible viscoelastic materials. In: Proceedings of the 19th JSME computational mechanics conference, Nagoya, Japan, pp 45–46 (in Japanese)
14. Okada J, Hisada T (2009) Study on compressibility control of hyperelastic material for homogenization method using mixed finite element analysis. J Comput Sci Technol 3(1):89–100
15. Okada J, Washio T, Hisada T (2009) Nonlinear homogenization algorithms with low computational cost. J Comput Sci Technol 3(1):101–114
16. Miehe C, Schroder J, Schotte J (1999) Computational homogenization analysis in finite plasticity. Simulation of texture development in polycrystalline materials. Comput Methods Appl Mech Eng 171:387–418
17. Allaire G (1992) Homogenization and two-scale convergence. SIAM J Math Anal 23:1482–1518
18. Terada K, Kikuchi N (2003) Introduction to the method of homogenization. Maruzen (in Japanese)
19. Yamada T, Matsui K (2007) Numerical procedure for nonlinear multiscale problems based on block Newton method. Proc Conf Comput Eng Sci 12:309–312 (in Japanese)

SIAM REVIEW
Vol. 52, No. 4, pp. 717–743



# A Parallel Multilevel Technique for Solving the Bidomain Equation on a Human Heart with Purkinje Fibers and a Torso Model*

Takumi Washio†
Jun-ichi Okada†
Toshiaki Hisada‡

**Abstract.** In this paper, we present a multigrid method and its implementation on parallel computers to solve the bidomain equation that appears in excitation propagation analysis of the human heart with the torso. The bidomain equation is discretized with the finite element method on a composite mesh composed of a fine voxel mesh around the heart and a coarse voxel mesh covering the torso. The extracellular potential problem on the torso is formulated as a variational problem with a constraint at the interface of the fine and coarse meshes. We show that this formulation naturally satisfies the conservation property of the electric currents and fits into the multilevel adaptive solution technique framework. We also present our special treatment of the Purkinje fiber network in the multigrid algorithm where it is modeled as multiway branching lines connected to the nodes in the voxel mesh of the heart. A parallel implementation of the proposed multigrid algorithm on distributed memory computers is presented and its performance is evaluated using real-life applications.

**Key words.** bidomain equation, excitation propagation, torso, multigrid, composite mesh

**AMS subject classifications.** 65N50, 65N30, 92C30

**DOI.** 10.1137/100798429

## 1. Introduction.

The bidomain equation is a widely accepted mathematical model for describing the excitation propagation and external stimulation of heart tissue [18, 23]. It consists of two partial differential equations (PDEs) coupled to ordinary differential equations (ODEs). The two PDEs describe the intra- and extracellular electrical circuits, respectively, that are separated by cell membranes. The ODEs incorporate the behavior of the cell membranes (capacitance of the membrane and the switching of several kinds of ion channels) to determine the currents between the two circuits. A simplified representation of this bidomain equation can be seen in Figure 1.1. The upper panel shows an array of cardiac myocytes which are electrically connected to each other by gap junctions and are surrounded by the extracellular

*Published electronically November 8, 2010. This paper originally appeared in *SIAM Journal on Scientific Computing*, Volume 30, Number 6, 2008, pages 2855–2881, and was supported by Core Research for Evolutional Science and Technology, Japan Science and Technology Agency.
http://www.siam.org/journals/sirev/52-4/79842.html

†Graduate School of Frontier Sciences, University of Tokyo, 5-1-5 Kashiwanoha, Kashiwa, Chiba, 277-0882, Japan (washio@sml.k.u-tokyo.ac.jp, okada@sml.k.u-tokyo.ac.jp).

‡Graduate School of Frontier Sciences, University of Tokyo, 7-3-1 Hongo, Bunkyo-ku, Tokyo, 113-0033, Japan (hisada@mech.t.u-tokyo.ac.jp).

liquids. Due to the capacitance effect of the cell membranes (red lines), there are discontinuities of the electrical potential field across the membranes in this microscopic view. In the bidomain equation, an electrical analogy of this situation is made as depicted in the lower left panel of Figure 1.1. Here, we assume that there are two continuous potential fields, one for the extracellular potential $\phi_e$ and the other for the intracellular potential $\phi_i$, which are separated by the capacitor (cell membranes) and connected by the ion channels. We also assume that the intracellular and extracellular potential fields are connected by the conductances corresponding to the gap junctions and the extracellular liquids, respectively. As the conductance inside the myocyte is much larger than that of the gap junctions, it can be ignored for the intracellular potential field. For computation of the ion channel current $I_{ion}$, the Luo–Rudy model [13] and the Noble model [21] have been implemented for ventricular myocytes, while the Nattel model [6] was used for atrial myocytes in our simulator. For example, the majority of ion channel currents in the Luo–Rudy model are given as

$$I_{ion} = I_{Na} + I_{Si} + I_K + I_{K1} + \cdots, \tag{1.1}$$

$$I_{Na} = \bar{g}_{Na} \cdot m^3 \cdot h \cdot j \cdot (V_m - E_{Na}), \tag{1.2}$$

$$I_{Si} = \bar{g}_{Si} \cdot d \cdot f \cdot (V_m - E_{Si}), \ldots, \tag{1.3}$$

where $I_{Na}$, $I_{Si}$, $I_K, \ldots$ are the electrical currents through the individual ion channels driven by the differences of the transmembrane potential $V_m = \phi_i - \phi_e$ and the potentials in the equilibrium for the individual ions $(E_{Na}, E_{Si}, \ldots)$. The coefficients of these potential differences are given by the products of the maximal values of the conductances $(\bar{g}_{Na}, \bar{g}_{Si}, \ldots)$ and the gating variables $(m, h, j, d, f, \ldots)$. A gating variable $x$ is time-varying and is governed by the differential equation

$$\frac{dx}{dt} = \alpha_x(V_m)(1 - x) - \beta_x(V_m)x, \tag{1.4}$$

where the functions $\alpha_x$ and $\beta_x$ are given for each gating variable $x$. Note that there are other types of ion channel currents that depend on the intracellular ion concentrations. Further, there are more complex models in which some ion channels are influenced by the metabolic reactions [5] and mechanical stimulations [11]. Our heart simulator (UT heart simulator [24]) attempts to integrate these electrophysiological phenomena and couple them with the mechanical function of the heart as a blood pump. In cardiac myocytes, $Ca^{2+}$ plays an important role in electrical activity and in controlling the contraction force of myofibrils. As depicted in the lower right panel of Figure 1.1, $Ca^{2+}$ release and uptake at the sarcoplasmic reticulum (SR) are also incorporated in the aforementioned cardiac myocyte models.

In this paper, we utilize the bidomain equation in which the geometries and material properties of the heart and the torso are incorporated. As depicted in Figure 1.2, let $\Omega_H$ be the domain of the heart muscle and $\Gamma_H$ the boundary of $\Omega_H$. The explanations for the subdomains $\Omega_C$ and $\Omega_P$ outside $\Omega_H$ are given later in this section. The bidomain equation for the intracellular potential $\phi_i$ and the extracellular potential $\phi_e$ coupled through the transmembrane potential $V_m = \phi_i - \phi_e$ on the heart muscle is given by

$$-\nabla \cdot \boldsymbol{\sigma}_i \nabla \phi_i = -\beta I_m \text{ on } \Omega_H, \tag{1.5}$$

$$\vec{n}_H \cdot \boldsymbol{\sigma}_i \nabla \phi_i = 0 \text{ on } \Gamma_H, \tag{1.6}$$

$$-\nabla \cdot \boldsymbol{\sigma}_e \nabla \phi_e = \beta I_m \text{ on } \Omega_H, \tag{1.7}$$

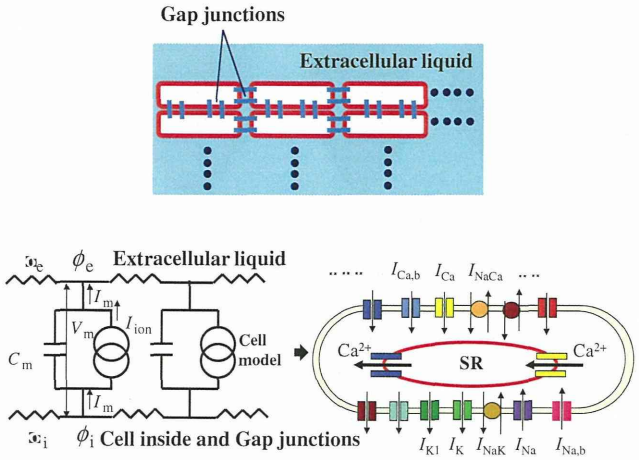


**Fig. 1.1** *The array of cardiac cells (upper panel), its electrical analogy (lower left panel), and the ion channels at the cell membrane and at the SR inside the cell (lower right panel).*

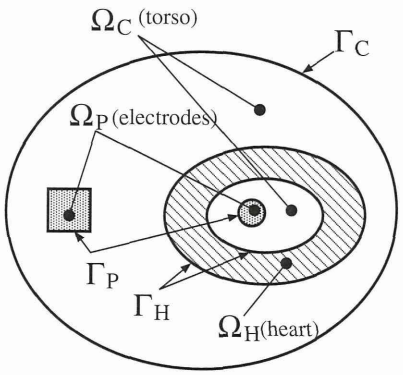


**Fig. 1.2** *Two-dimensional image of the heart domain $\Omega_H$, the torso outside the heart $\Omega_C$, the electrodes $\Omega_P$, and their boundaries.*

$$\vec{n}_H \cdot \boldsymbol{\sigma}_{\mathrm{e}} \nabla \phi_{\mathrm{e}} = J_H \text{ on } \Gamma_H, \tag{1.8}$$

$$I_{\mathrm{m}} = C_{\mathrm{m}} \frac{\partial V_{\mathrm{m}}}{\partial t} + I_{\mathrm{ion}}(V_{\mathrm{m}}, \boldsymbol{S}) \text{ on } \Omega_H. \tag{1.9}$$

Here, $\boldsymbol{\sigma}_{\mathrm{i}}$ and $\boldsymbol{\sigma}_{\mathrm{e}}$ are the intra- and extracellular conductivity tensors, respectively, $\beta$ is the surface-to-volume ratio of the tissue, $C_{\mathrm{m}}$ is the membrane capacitance per unit area, and $I_{\mathrm{m}}$ is the transmembrane current per unit area. The transmembrane current $I_{\mathrm{m}}$ is a combination of a capacitive current $C_{\mathrm{m}} \partial V_{\mathrm{m}} / \partial t$ and an ionic current $I_{\mathrm{ion}}(V_{\mathrm{m}}, \boldsymbol{S})$ passing through several kinds of ion channels, where $\boldsymbol{S}$ is a state vector composed of gating variables. $J_H$ is a current entering the extracellular domain of the heart through $\Gamma_H$, and $\vec{n}_H$ is the outward normal vector on $\Gamma_H$.

The intra- and extracellular conductivity tensors of the myocardium (heart muscle) are anisotropic. They are given by

$$\boldsymbol{\sigma} = c_f \boldsymbol{n}_f \otimes \boldsymbol{n}_f + c_s \boldsymbol{n}_s \otimes \boldsymbol{n}_s + c_n \boldsymbol{n}_n \otimes \boldsymbol{n}_n, \tag{1.10}$$

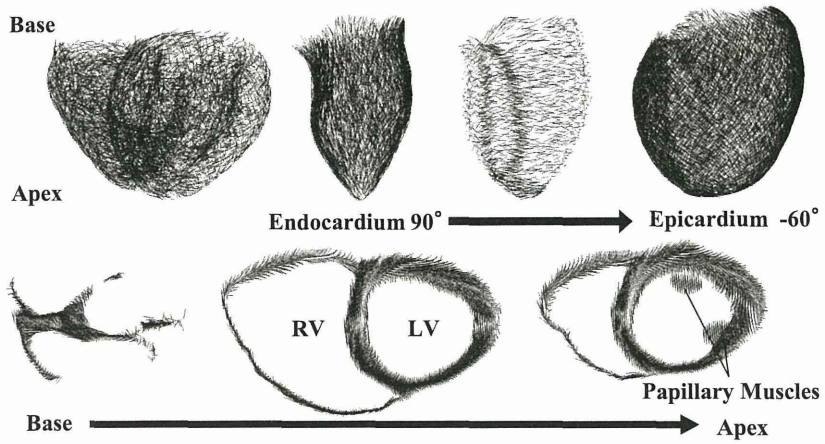


**Fig. 1.3** *Fiber directions in the ventricles. The orientation of a fiber varies from $+90°$ to $-60°$ relative to the circumferential direction in a plane perpendicular to the transmural direction from the endocardiac to the epicardiac layer.*

**Table 1.1** *Conductivities [mS/cm] of the myocardial cells and the surface-to-volume ratio of the tissue $\beta$ [1/cm].*

| Cells | Intra $(f, s, n)$ | Extra $(f, s, n)$ | $\beta$ |
|---|---|---|---|
| Ventricle | 7.2, 2.4, 2.0 | 6.0, 3.0, 3.0 | 2000 |
| Atrium | 7.0, 7.0, 7.0 | 7.0, 7.0, 7.0 | 2000 |

where $\boldsymbol{\sigma} = \boldsymbol{\sigma}_{\mathrm{i}}$ or $\boldsymbol{\sigma}_{\mathrm{e}}$. Here, $\boldsymbol{n}_f, \boldsymbol{n}_s$, and $\boldsymbol{n}_n$ denote the fiber, sheet, and sheet-normal directions, respectively, in the orthonormal basis [9]. The bases vary depending on the position in the heart. In general, the conductivity along the fiber direction $c_f$ is the largest of the three. The orientations of the myocytes (fiber directions) have been modeled based on anatomical observations. Figure 1.3 depicts the distributions of the fiber directions in our simulation. The muscle fibers have a helical structure within the left ventricle (LV). Based on histological studies, fiber directions can be determined as the orientation of a fiber varies from $+90°$ to $-60°$ relative to the circumferential direction in a plane perpendicular to the transmural direction from the endocardiac to the epicardiac layer, resulting in a very realistic model for the fiber directions. Table 1.1 gives the conductivities in the three directions and the surface-to-volume ratio for our simulations. These conductivities are at least two times larger than the standard values. Due to the limitation of our computational resources, the local mesh size is set to 0.4 mm, which is still too large to obtain a proper wave propagation velocity (less than 0.1 mm is required). The conductivities have therefore been adjusted in order to obtain a usable wave propagation velocity.

Strong demands from physiological application areas require three-dimensional simulations to include the torso surrounding the heart as well. Physically, cardiac electrical activity results in a current flow in the torso via the extracellular potential field. Thus, the extracellular PDE should be extended from the heart to the torso via the boundary current $J_H$ in (1.8).

One of the applications that requires the torso model is the simulation of an implantable cardioverter defibrillator (ICD) [12]. This device delivers a strong electrical shock to the heart through the electrodes when a fatal arrhythmia is detected, as

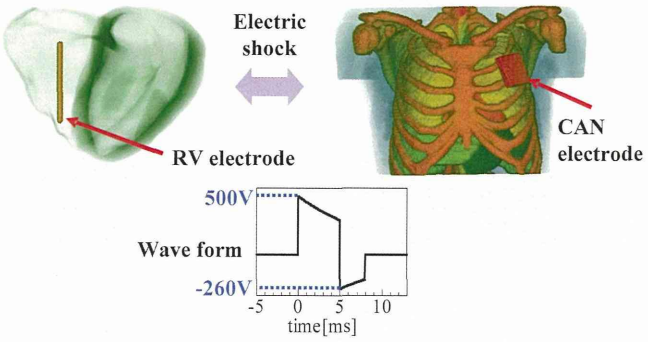


**Fig. 1.4** *Two electrodes of an ICD and a typical voltage profile between them.*

depicted in Figure 1.4. By optimizing the arrangement of electrodes and the temporal profile of the electrical current, an ICD can be developed that is much more comfortable than the device currently used.

The other important application is a simulation of the electrocardiogram (ECG) routinely used in clinical practice. In order to reproduce the ECG based on the real physiological system, modeling of the so-called Purkinje fiber network is indispensable. The Purkinje fibers are located on the inner ventricular walls of the heart with large free-running sections. They are some of the specialized cardiac muscle fibers that form the impulse-conducting network of the heart, and they transmit impulses rapidly from the atrioventricular node to the ventricles. In our simulator, the DiFrancesco–Noble cell model [7] is used for the Purkinje fibers and the network is modeled from the atrioventricular node to the myocardium. With this model, we can analyze the relations between the body surface potential and the excitation propagation in the heart in a healthy condition and in various conditions involving heart disease. This research, therefore, contributes to early recognition and treatment through diagnosis with an ECG. Furthermore, a mechanism of arrhythmia that originates from the Purkinje fiber network, and the impact of the Purkinje fiber network at defibrillation, can be clarified by these simulations. Figure 1.5 shows the first half of one normal heartbeat as computed by our simulator. In the upper part, the membrane potentials on the Purkinje fiber and the heart muscle, as well as the body surface potentials, are depicted at typical times. At the bottom of the figure, the second-lead ECG obtained from this computation is depicted. This agrees well with actual clinical observations.

In our heart simulator, mechanical simulation of the beating heart, including intracavitary blood flow and movements of valve leaflets, can be also performed using the fluid-structure interaction finite element method [34, 35] (see Figure 1.6). In this simulation, the $Ca^{2+}$ concentration data obtained from our electrophysiology model is applied to an excitation-contraction coupling model of sarcomere dynamics to compute the contraction force of every finite element of the heart muscle mesh. This results in the synchronous contraction of the heart and blood ejection. Thus far, we have been able to retrieve and present the time courses of intracavitary volumes and blood pressures and so forth for both healthy and diseased hearts. Such a simulation allows us to examine the influence of various electrophysiological phenomena on the mechanics of the heart [24].

The mathematical formulation for the extension of the extracellular potential equation to the torso is given as follows. As depicted in Figure 1.2, let $\Omega_C$ be the